PCCP

PAPER

Defect mediated magnetic transitions in Fe and Mn doped MoS_2

Cite this: DOI: 10.1039/c8cp02882f

Manish Kumar Singh,[a] Prajwal Chettri,[b] Ajay Tripathi,[b] Archana Tiwari,[b] Bratindranath Mukherjee[a] and R. K. Mandal*[a]

Received 6th May 2018,
Accepted 17th May 2018

DOI: 10.1039/c8cp02882f

rsc.li/pccp

We report single-phase syntheses of undoped 2H-MoS_2 as well as Mn and Fe doped MoS_2 by a facile hydrothermal route. The formation of the 2H-MoS_2 phase was confirmed by XRD and was corroborated with Raman spectra. The morphology of the doped and undoped MoS_2 nanostructures comprised sheets, as revealed by TEM and STEM images. The fine granular structure was observed by high resolution TEM micrographs. The STEM-EDS results show dopant concentrations of ~1 atom% corresponding to Mn and Fe in doped MoS_2. The undoped MoS_2 revealed diamagnetic behavior at room temperature and paramagnetic behavior in the range (100 to 300 K). The Mn-MoS_2 sample displayed ferromagnetism below 20 K with a coercive field of ~50 O_e. Such a sample may be utilized for magnetic switching purposes at low temperatures. The onset of the antiferromagnetic interaction was observed below 145 K in Fe-MoS_2 samples. They have been understood in terms of long-range magnetic interactions amongst the dipole moments mediated *via* surface defects as well as the interaction between the dipoles and the surface charges. The findings are corroborated with the help of EPR studies.

1. Introduction

Transition metal dichalcogenides (TMDCs) have received considerable attention from researchers owing to their applications in the areas of optoelectronics, electronics, photo catalysts, magnetic switching and storage.[1–9] Molybdenum disulfide (MoS_2) in particular with a direct band gap is a suitable candidate for optoelectronic and photo catalytic applications.[10–12] The ease of doping and heterostructure formation with tunable and desired properties make it an attractive alternative to graphene.[13] 2H-MoS_2 in its bulk form is semiconducting in nature and doping with transition metals such as Fe, Ni, Co, and Mn makes it a promising candidate for dilute magnetic semiconductors (DMS).[4,9,14–18] Nanostructural manipulations *via* grain and grain boundary engineering might open an avenue to tailor the magnetic properties of transition metal doped MoS_2.[19] In this study, we have synthesized MoS_2, Fe and Mn doped MoS_2 by a hydrothermal method.

Unlike previous studies where MoS_2 is reported to be ferromagnetic in nature,[3,5,15,20–22] we could synthesize single-phase MoS_2 powders with a diamagnetic character. It may be noted that ferromagnetic characteristics in MoS_2 have been observed for thin films deposited over substrates. In this investigation, we also demonstrate the effect of Fe and Mn dopants in MoS_2 on their magnetic behavior. It is well known that in their atomic/ionic form Fe and Mn display long-range ferromagnetic and anti-ferromagnetic ordering, respectively, owing to the Heisenberg exchange interaction. However, we found reversal of their magnetic behaviors in doped samples of MoS_2. This is perhaps the most interesting part of our investigation. The undoped MoS_2 revealed diamagnetic behavior at room temperature and paramagnetic behavior in the range (100 to 300 K). The Mn-MoS_2 sample displayed ferromagnetism below 20 K with a coercive field of ~50 O_e. The onset of antiferromagnetic interaction was observed below 145 K in Fe-MoS_2 samples. This has been understood in terms of long-range magnetic interactions amongst the dipole moments mediated *via* surface defects as well as the interaction between the dipoles and the surface charges. It will be shown that magnetic behavior in this investigation has arisen thanks to doping, as we are dealing with a single-phase material with structural nano domains of similar lengths.

2. Synthesis methods

The MoS_2 nanostructures were synthesized by a hydrothermal method. In this, 1 millimole of ammonium heptamolybdate (AHM) was mixed in 30 mL of de-ionized water and stirred

[a] Department of Metallurgical Engineering, Indian Institute of Technology (BHU), Varanasi-221005, Uttar Pradesh, India
[b] Department of Physics, School of Physical Sciences, Sikkim University, Gangtok-737102, Sikkim, India

magnetically to get a clear solution. Into this solution 28 millimoles of thiourea were added and stirred until complete dissolution. The above solution was transferred into a 50 mL Teflon-lined hydrothermal autoclave reactor and placed in a Muffle furnace at 220 °C for 18 h. The reaction product was cleaned by centrifugation and ultrasonication cycles using DI water and finally with ethanol. The product was vacuum dried at 60 °C to obtain a black-colored powder. $FeCl_3{\cdot}3H_2O$ and $MnSO_4$ precursors from Alfa Aesar were utilized for the synthesis of Fe and Mn doped MoS_2, respectively. The doping of ~3 atom per cent of these transition metals required the addition of 0.21 millimoles of dopant precursors into AHM and thiourea solution. The resulting solutions were stirred magnetically to achieve homogeneity. The remaining procedures were the same as those for the synthesis of MoS_2.

3. Instrumentation

The prepared undoped, Mn and Fe doped MoS_2 powders were investigated at room temperature using a PANanalytical X. Pert Pro-X-ray diffractometer (XRD) with Ni-filtered Cu K_α radiation of wavelength 1.54 Å. A Renishaw inVia RM2000 Raman spectrometer was used to collect the Raman spectra for undoped, Mn, and Fe doped MoS_2 using a 785 nm excitation wavelength, a 50× objective, and 10 seconds exposure time; the power used was 1 per cent. Transmission electron microscopy (TEM) investigations and scanning TEM-energy dispersive X-ray spectroscopy (STEM-EDS) characterization were carried out with FEI, Tecnai G^2T20 and Talos F200X microscopes operating at 200 kV. Room-temperature electron paramagnetic resonance (EPR) measurements were performed on a Bruker A200X-band CW spectrometer using 9.83 GHz microwave frequency, 8 mW microwave power and 10 G modulation amplitude. The EPR parameters were evaluated by simulating the experimental spectra using EASYSPIN.[23] Magnetic hysteresis and susceptibility were recorded using Quantum Design SQUID-VSM. The magnetic field was zeroed before every measurement from an initial +10 Oe in an oscillating mode at room temperature. This was done in order to minimize the effects of a trapped magnetic field in the SQUID.

The phase and the nature of the layered structure were determined by XRD and Raman spectroscopy, respectively. The morphologies and lattice structures were investigated with TEM and electron diffraction patterns. The STEM-EDS was carried out for micro-chemical analysis of Fe and Mn doped MoS_2 samples. The magnetic response was studied in terms of magnetization by varying the temperature from 300 K to 5 K. The data was collected in the Zero Field Cooling (ZFC) and Field Cooled Cooling (FC) modes of measurement.

4. Results and discussion

4.1. Structural characterization

Fig. 1 shows the XRD pattern of undoped, Mn doped, and Fe doped MoS_2 nanostructures with the standard XRD pattern of

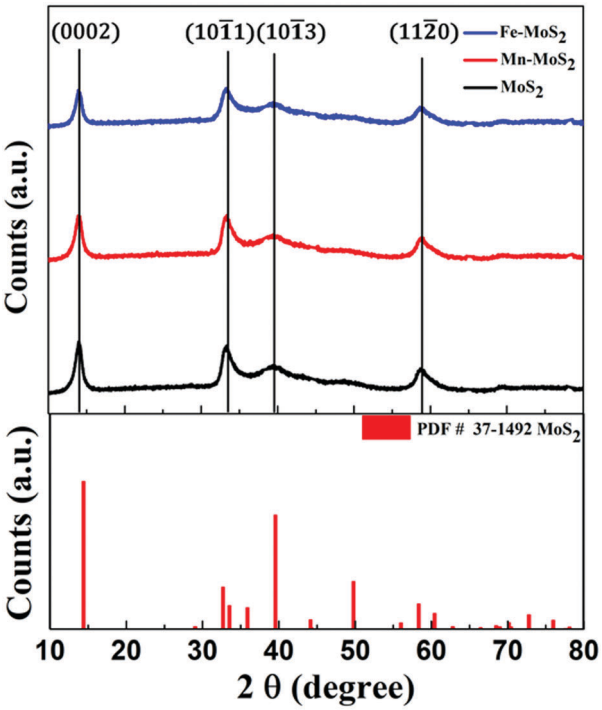

Fig. 1 Powder X-ray diffraction patterns of MoS_2, Mn doped MoS_2 and Fe doped MoS_2 nanostructures. The bottom figure shows the standard XRD patterns of 2H-MoS_2 (PDF #37-1492).

MoS_2 (bottom figure). The reflections (0002), (10$\bar{1}$1), (10$\bar{1}$3) and (11$\bar{2}$0) corresponding to 2H-MoS_2 (PDF #37-1492) were observed. The absence of additional peaks in the XRD pattern of Mn and Fe doped MoS_2 rule out the possibilities of formation of their sulfide phases. Moreover, the Mn and Fe doped MoS_2 patterns do not show a significant change in the disposition of the peaks compared to that of undoped MoS_2. This may be attributed to the dilute addition of Mn and Fe dopants in the MoS_2. It may be noted that under the present synthesis conditions (with variable pH and S^{2-} concentrations) sulfide formation of the dopants is more favorable compared to their unreacted soluble salts. This in turn rules out the possibility of removal of dopants ions during the subsequent washing protocol. Therefore, dopants are incorporated into the MoS_2 lattice and a single-phase Mn and Fe doped MoS_2 has formed. The Scherrer formula was used to measure the crystallite size of the undoped and doped MoS_2 samples. The crystallite sizes corresponding to the (10$\bar{1}$1), (10$\bar{1}$3) and (11$\bar{2}$0) reflections of the undoped, Mn, and Fe doped MoS_2 samples are estimated to be ~8.0 nm, 5 nm, 3 nm, and 3 nm, respectively. Since MoS_2 is a layered material, as confirmed by our TEM results (to be presented later), and (0002) is the axis normal to the layer, which suggests that the average thickness of the as-synthesized nanostructures is ~7 monolayers. Fig. 2 displays the Raman spectra of undoped, Mn doped and Fe doped MoS_2 nanostructures. The characteristics peaks at the ~384 cm^{-1} and ~408 cm^{-1} positions correspond to the E_{2g} and A_{1g} vibration modes of the phonon, suggesting that the undoped synthesized MoS_2 nanostructures is 2H-MoS_2.[24] Doping with Mn and Fe in MoS_2 did not

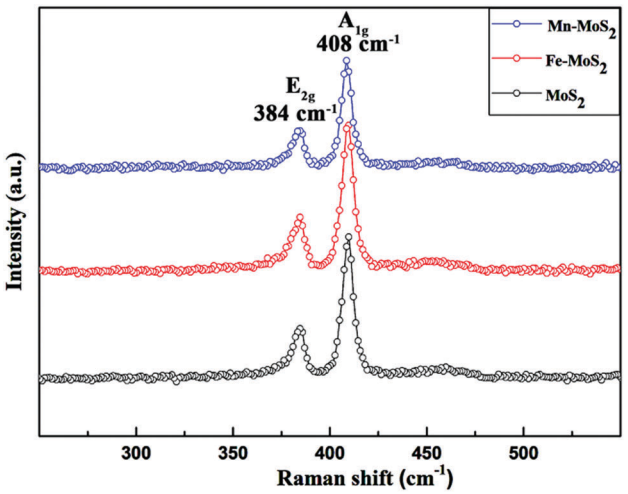

Fig. 2 Raman spectra of the undoped, Mn doped, and Fe doped MoS_2 single 2H-MoS_2 phase. The characteristics peaks at positions at ~384 cm^{-1} and ~408 cm^{-1} corresponding to the E_{2g} and A_{1g} modes of phonon vibrations are shown.

reveal any additional peak in the Raman spectra conforming once again to the dilute addition of dopants into MoS_2.[9] From the XRD and Raman results, we conclude that both undoped and doped MoS_2 nanostructures display a single 2H-MoS_2 phase.

Fig. 3 shows a high resolution TEM (HRTEM) micrograph of Mn doped MoS_2, with insets of the Fast Fourier Transform (FFT) in the bottom right as well as a magnified view of the selected region in the top left. The presence of a thin layer and several layers of Mn doped MoS_2 is shown with arrows. The FFT revealing reflections corresponding to $(10\bar{1}1)$ of 2H-MoS_2 is depicted in the micrograph. The magnified image from the selected region shows nanocrystalline domains with an average size of $\sim 1.3 \pm 0.3$ nm (averaged over at least 35 regions chosen statistically). Two such domains are depicted by putting false colors (red and green) on them.

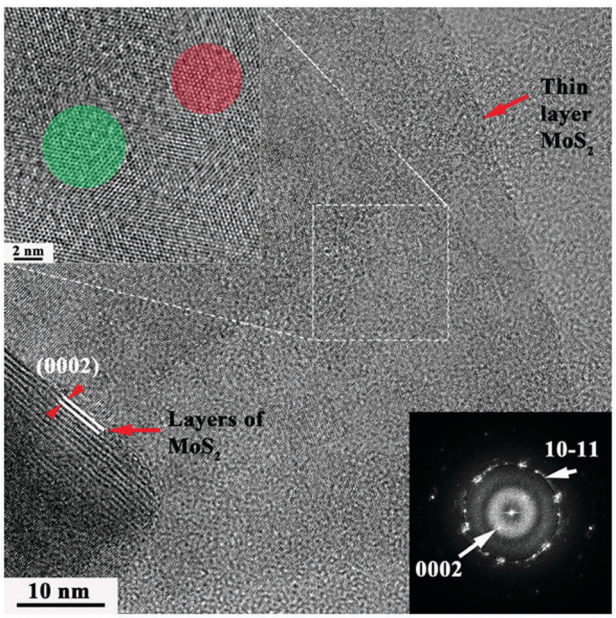

Fig. 3 HRTEM micrograph with FFT as inset (bottom right) displays spots corresponding to the (0002) and $(10\bar{1}1)$ planes of 2H-MoS_2. Arrows (top right and bottom left) show thin layers of 2H-MoS_2. The magnified HRTEM image (inset top left) of the selected region of this (white square) depicts the crystalline domains. Two such domains are highlighted using false color. The (0002) plane of 2H-MoS_2 is also shown in the figure.

Fig. 4 displays the STEM-HAADF-EDS elemental maps of Mo, S, and Mn. The HAADF image (Fig. 4a) shows the sheet-like morphology of the Mn-MoS_2 nanostructures. Maps display the uniform distribution of Mo, S, and Mn. Further, the absence of clusters in the elemental map of Mn rules out the possibility of Mn-sulfide phases. Therefore, Mn has been distributed uniformly in 2H-MoS_2 and a single phase has formed. The elemental compositions of Mn, Mo, and S were found to be ~1 atom%, ~32 atom%, and ~65 atom%, respectively.

The bright field TEM image and corresponding selected area diffraction pattern of Fe doped MoS_2 are shown in Fig. 5. A flower-like morphology was observed and is comprised of buckled sheets of MoS_2. The diffraction rings are indexed as $(10\bar{1}1)$, $(10\bar{1}3)$ and (0008) reflections of 2H-MoS_2 phases (PDF #37-1492). The appearance of diffuse rings indicates the presence of fine crystalline nano domains in the sample. Fig. 6 displays the STEM-HAADF-EDS elemental maps of Mo, S, and Fe in Fe-MoS_2 in Fig. 6c, d and e, respectively. The distributions of the elements are uniform in the sheets, conforming to the single phase. The HRTEM micrographs of the Mn and Fe doped MoS_2 are shown in Fig. 7. The FFTs (given in the inset) are comprised of streaks in the spots, indicating that the nanocrystalline structural domains are misoriented from each other but the angle of misorientation appears to be very small. Hence, nanocrystalline domains are observed in both Mn and Fe doped MoS_2. Unlike all previous reports, we are dealing with the dilute addition of antiferromagnetic (Mn) and

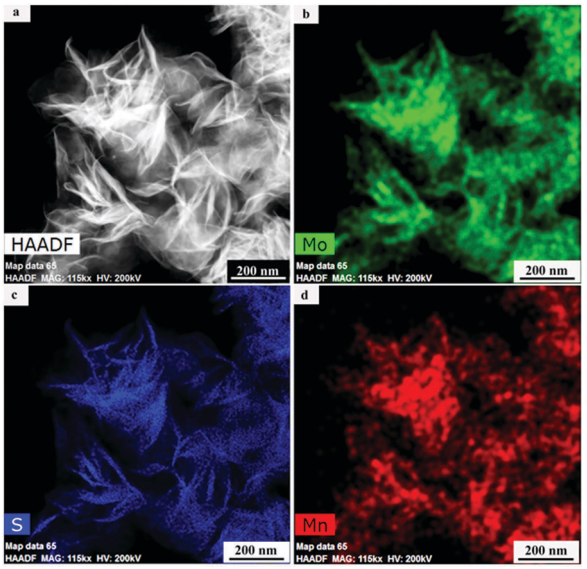

Fig. 4 STEM-HAADF-EDS elemental mapping of Mn doped MoS_2. High angle annular dark field (HAADF) image (a) and elemental maps corresponding to Mo (b), S (c), and Mn (d), respectively.

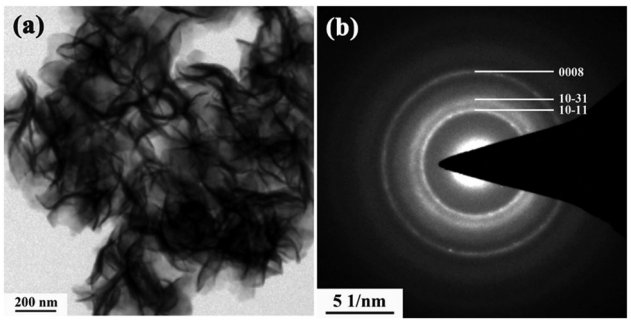

Fig. 5 Bright field TEM micrograph of Fe doped MoS_2 (a) and corresponding selected area diffraction pattern (b).

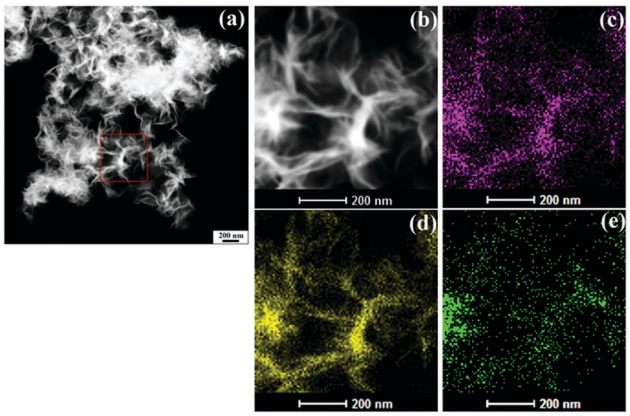

Fig. 6 Scanning TEM-HAADF image of Fe doped MoS_2 (a), HAADF image of the selected area (b), elemental maps corresponding to Mo (c), S (d), and Fe (e), respectively.

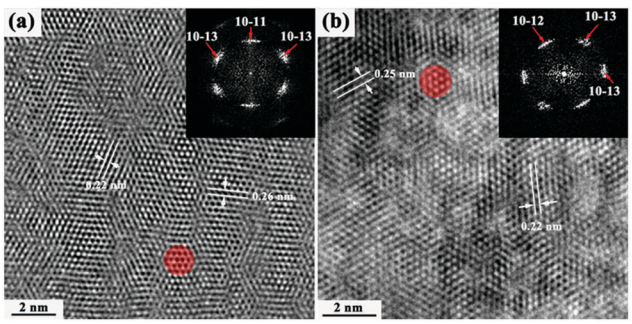

Fig. 7 HRTEM micrographs of Mn doped MoS_2 (a) and Fe doped MoS_2 (b) with their FFTs as insets. The nano domains are shown by applying false colors in the micrographs.

ferromagnetic (Fe) elements as well as a single phase. Hence, the formation of sulfide phases is ruled out *a priori*. In view of this, we conclude that all the dopants have gone into the planar hexagonal net of MoS_2. This was substantiated by our XRD, Raman spectra, HRTEM and STEM-EDS results.

4.2. Magnetic characterization

The magnetic response of MoS_2 powder used in the present study shows diamagnetic behavior (*cf.* Fig. 8a). Unlike previous

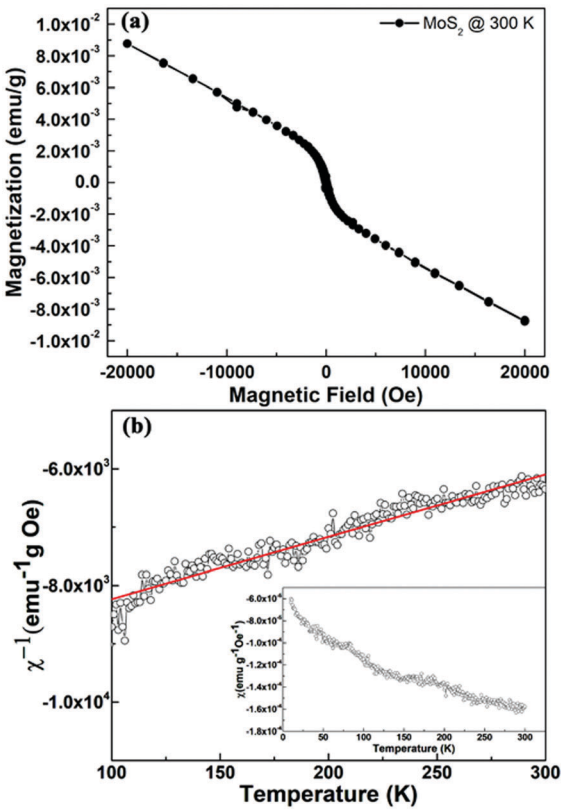

Fig. 8 (a) Magnetization *versus* magnetic field loop for MoS_2 at 300 K revealing the diamagnetic character of the sample, (b) inverse of magnetic susceptibility (χ^{-1}) *versus* temperature of MoS_2 powder where the data fits linearly with the Curie law. The inset shows the magnetic susceptibility (χ) *versus* temperature plot of MoS_2 powder measured at 100 O_e.

reports where a ferromagnetic hysteresis loop is evident on top of the diamagnetic background in MoS_2 films, this powder presented pure diamagnetic behavior without any long-range ordering. This could be attributed to the negligible ferromagnetic signal arising from the edges or vacancies in the bulk limit of MoS_2. The diamagnetic susceptibility of MoS_2 is also examined by varying the temperature and is plotted in Fig. 8(b). Unlike a pure diamagnetic material where temperature-independent diamagnetic susceptibility is observed, we find temperature-dependent behavior, which is shown in Fig. 8(b). By plotting the inverse of the susceptibility (χ) as a function of temperature, linear Curie–Weiss law behavior is observed between 100 K and 300 K. This could be ascribed to the presence of a few paramagnetic centers in MoS_2. As for the fitting parameters, the Curie constant C is found to be 9.6×10^{-4} emu K g^{-1} Oe^{-1} and the Weiss temperature T_c is found to be $\sim$885 K. The presence of a high and positive T_c in MoS_2 is in agreement with previous reports where magnetization is observed due to diamagnetic, paramagnetic and ferromagnetic interactions arising from different types of defects.[25] The result is in conformity with the weak EPR lines of the MoS_2 sample exhibiting uniaxial g-anisotropy with $g_{\parallel} = 2.010$ and $g_{\perp} = 2.002$ (see Fig. 9). Similar g-values have been reported previously for MoS_2 samples and attributed to sulfur (S)-related defects at the

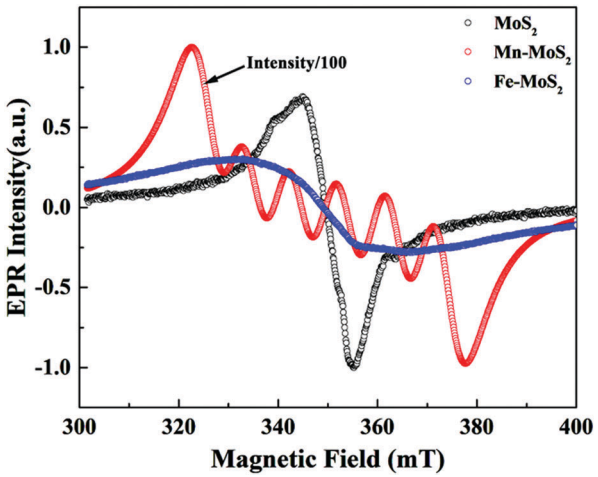

Fig. 9 EPR spectra of undoped, Mn, and Fe doped MoS_2 samples. The undoped MoS_2 displays uniaxial anisotropy in *g*, Mn-MoS_2 depicts an enhanced signal accompanied by hyperfine splitting, and Fe-MoS_2 shows isotropy in *g* with reduced signal intensity. The arrow shows the EPR signal corresponding to Mn-MoS_2 which is scaled by 100 to fit into the intensity range of the undoped and Fe-MoS_2 samples.

poor symmetry sites/edges of nanocrystalline MoS_2. The other high field weak EPR lines could be due to Mo-related local defects arising either from the dangling bonds or dislocations.[26] It may be pointed out that the TEM micrographs do show a sheet-like morphology in this investigation. However, magnetic measurements from powder samples mask its individual contribution.

The magnetization of Mn-MoS_2 is plotted as a function of magnetic field at different temperatures in Fig. 10(a). It can be noted from the figure that at 300 K, the sample is diamagnetic whereas it becomes paramagnetic at 50 K and by further lowering the temperature to 20 K, it behaves like a ferromagnet with a small coercive field of $\sim$50 O_e. In order to understand the thermal ordering in the sample, the temperature-dependent susceptibility of Mn-MoS_2 and its inverse are given in Fig. 10(b) and (c). Three dominant phase transitions can be noted from the figure. These refer to the temperature ranges (i) 23–300 K, where the magnetic susceptibility is fairly small and constant, (ii) 40–230 K, where the susceptibility increases by lowering the temperature (Curie–Weiss law) and (iii) below 35 K, where a sharp increase in χ is observed for both ZFC and FC modes. Further, to elaborate the observed transitions, the temperature range (70–230 K) is fitted with the Curie–Weiss law (see Fig. 10(c)). The observed Curie constant *C* is $\sim 6.43 \times 10^{-5}$ emu K g^{-1} O_e^{-1} and T_c is $\sim$55 K. The T_c value suggests that there exists a weak ferromagnetic phase along with the paramagnetic background in Mn-MoS_2. As the free Mn ions are paramagnetic by nature, the presence of weak ferromagnetism can be warranted due to exchange interaction between free electrons on Mn ions and surface charges on MoS_2 arising due to S-vacancy.[9] These charges align around Mn-ions and thus give rise to the ferromagnetic coupling. Interestingly, by further lowering the temperature, the χ value bifurcates for ZFC and FC curves at 30 K. Due to the presence of uncompensated surface

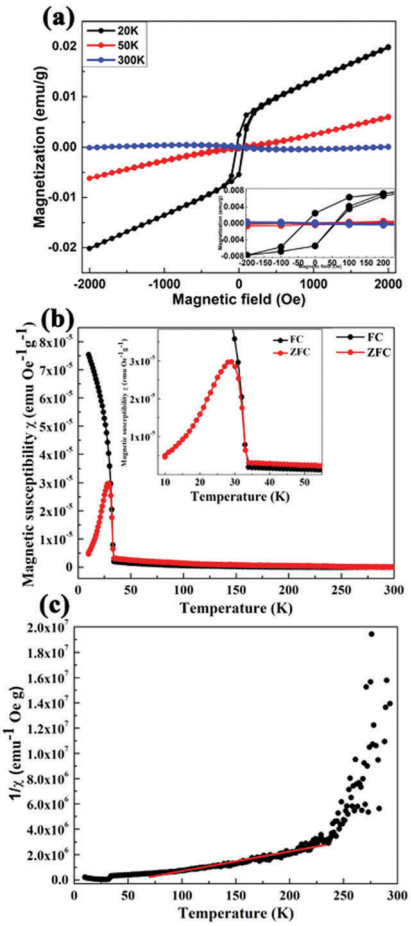

Fig. 10 (a) Magnetization *versus* magnetic field loop for Mn-MoS_2 revealing the diamagnetic character of the sample at 300 K, paramagnetism at 50 K and ferromagnetism at 20 K. The inset of the figure shows the enlarged hysteresis loop of the sample in the weak field regime. (b) Magnetic susceptibility (χ) *versus* temperature (between 5 K and 300 K) of Mn doped MoS_2 powder in both ZFC and FC cooled mode at 100 O_e and (c) $1/\chi$ *versus* *T* plot in the temperature range 5–300 K where the Curie–Weiss law is fitted in the range 70–230 K.

charges at low temperatures, bifurcation occurs, revealing the onset of another long-range interaction amongst Mn-ions and the surface charges. As reported previously, for nano domain sizes smaller than the magnetic exchange length, the local anisotropies are smoothed by the exchange interactions such that their effects are negligible on total magnetization. For such cases, in general, small coercive fields are observed.[27,28] The observed small coercivity in our case conforms to this, making Mn-MoS_2 a suitable soft magnet for magnetization reversal and memory storage applications.

In order to elucidate the room-temperature paramagnetic properties, the EPR spectrum of Mn-MoS_2 is also examined and is shown in Fig. 9. Like previous reports, we also observed the presence of six characteristic hyperfine lines of Mn^{2+} (I = 5/2) with axially anisotropic *g*-values 2.011 and 2.003 and hyperfine interaction constants 283 and 81 MHz.[9,29] The broad peak corresponding to S-vacancy is also observed in the background. Interestingly, the EPR signal is nearly two orders stronger in

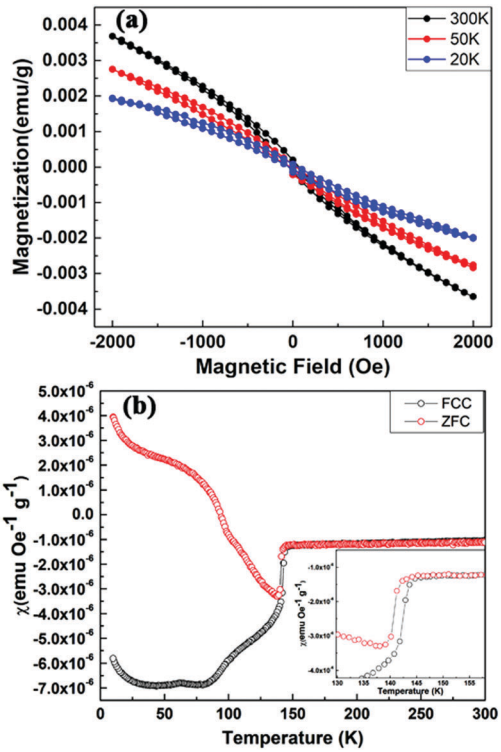

Fig. 11 (a) Magnetization *versus* magnetic field loop for Fe doped MoS_2 revealing the diamagnetic character of the sample at 20 K, 50 K and 300 K, (b) Magnetic susceptibility (χ) *versus* temperature (between 5 K and 300 K) of Fe-MoS_2 powder in both ZFC and FC mode at 100 O_e. The inset shows magnetic susceptibility (χ) *versus* temperature (between 120 K and 160 K) plot of Fe-MoS_2 powder, revealing the transition temperature around 145 K.

Mn-MoS_2 than that in MoS_2, suggesting that the surface charge densities on MoS_2 have been increased by the Mn substitution. These results corroborate the existence of a ferromagnetic interaction between the defect-related surface charges and the dopants at low temperatures. These results are in agreement with those of the XRD and Raman spectra, suggesting the substitution of Mn ions over the MoS_2 surface in a single phase. STEM-EDS results also substantiate these findings.

The room-temperature EPR spectrum of Fe-MoS_2 reveals the presence of a broad peak with an isotropic *g*-value $g = 2.015$ (*cf.* Fig. 9). The intensity of the EPR signal is nearly half of that of MoS_2, suggesting the randomization of the surface charges on MoS_2 and their local interactions with the dopants. The magnetization of the Fe-MoS_2 sample is also plotted as a function of magnetic field at different temperatures in Fig. 11(a). The sample shows diamagnetic behavior at 20 K, 50 K and 300 K with variable slopes and small coercive fields ($\sim$20 O_e). The observed behavior cannot be classified as purely diamagnetic nor weakly ferromagnetic, as both characters are evident from the hysteresis loops. In addition, lower saturation magnetization for Fe-MoS_2 is observed than that of Mn-MoS_2, which confirms the randomization of surface charges. There are relatively finer structural domains in Fe-MoS_2 ($\sim$1.1 nm) than Mn-MoS_2 ($\sim$1.3 nm) at the given temperature.[30,31] The weak magnetization in Fe-MoS_2 can be attributed to the preferred substitution of Fe ions on the S-edge over the Mo-edge of the MoS_2 sheets and the dominant diamagnetic background of the MoS_2 matrix.[8]

The temperature-dependent magnetic susceptibility of Fe-MoS_2 is plotted in both ZFC and FC modes and is shown in Fig. 11(b). The sample remains mainly diamagnetic in the temperature range 150–300 K. However, by further lowering the temperature, a sharp decrease in χ and its thermal hysteresis are noted at 145 K, revealing the onset of antiferromagnetic interactions amongst Fe ions and the local matrix. Below 138 K, the χ value bifurcates for the ZFC and FC modes. We attribute these thermally irreversible differences in the magnetization to the coexistence of antiferromagnetic and ferromagnetic interactions in the sample.[32,33] It is worth-mentioning that the effects of higher magnetic fields on the bifurcation magnitude and temperature need to be explored for a better understanding of the observed behavior. Previously, the small and negative ZFC moments under weak magnetic fields have been attributed as artefacts due to trapped magnetic fields.[34] In our case, the field was zeroed before every measurement from an initial +10 Oe in an oscillating mode at room temperature (as mentioned in section 3). According to Kumar and Yousuf,[34] this may introduce negatively trapped fields and consequently a negative ZFC magnetization could be observed. However, in our case, we have rather observed an increase in the ZFC magnetization than that of FC mode. We therefore rule out the possibility of any artefacts being present in the sample due to trapped magnetic fields.[34,35] The χ in ZFC mode is greater than that in the FC mode for Fe-MoS_2. This reveals that cooling of the sample under a magnetic field (100 O_e) is aligning the moments in the opposite direction to the applied magnetic field and thus a lower value of magnetization is observed for the FC mode than that of the ZFC mode. Further, we are dealing with a single-phase material with structural nano domains of $\sim$1.0 nm. This permits us to infer that the dilute addition of Mn and Fe is responsible for the observed magnetic responses. The extremely fine structural nano domains and substitution of dopants in the 2H-MoS_2 lattice create defects as well as surface charges. The complex interplay of defects and surface charges is leading to long-range magnetic interactions amongst the dipoles.

5. Conclusions

We have synthesized undoped and, Mn and Fe doped MoS_2 nanostructures by a hydrothermal method. The phase of undoped MoS_2 was found to be 2H-MoS_2, as revealed by XRD and Raman spectra. The absence of sulfide phases in Mn and Fe doped samples were confirmed by XRD, Raman spectra, and STEM-EDS results. The EPR result shows the presence of Mn^{2+} ions in the Mn-doped MoS_2 sample. The undoped MoS_2 showed diamagnetic behavior at room temperature convoluted with a feeble ferromagnetic response. It shows a paramagnetic nature in the temperature window (100 K to 300 K) with $T_c \sim 884$ K.

The presence of a high and positive T_c in MoS_2 could be attributed to the diamagnetic, paramagnetic and ferromagnetic interactions arising from different types of defects. The Mn-MoS_2 revealed ferromagnetic behavior (below 20 K) with a small coercive field of $\sim$50 O_e. The Fe-MoS_2 sample exhibited the onset of an antiferromagnetic interaction amongst Fe ions and the local matrix below 145 K. Thus, we have demonstrated a reversal in the magnetic response of Mn and Fe through their dilute addition in MoS_2 *vis-à-vis* their elemental magnetic behaviors. Thus, research on the dilute addition of different types of magnetic ions in MoS_2 holds promise for potential applications in magnetic switching at low temperature.

Conflicts of interest

There are no conflicts to declare.

Acknowledgements

Two of us (BM and PC) acknowledge the financial support under DST-Inspire faculty and student schemes.

Notes and references

1 Q. H. Wang, K. Kalantar-Zadeh, A. Kis, J. N. Coleman and M. S. Strano, *Nat. Nanotechnol.*, 2012, **7**, 699.
2 C. Ataca, H. Sahin, E. Akturk and S. Ciraci, *J. Phys. Chem. C*, 2011, **115**, 3934–3941.
3 S. Tongay, S. S. Varnoosfaderani, B. R. Appleton, J. Wu and A. F. Hebard, *Appl. Phys. Lett.*, 2012, **101**, 123105.
4 X. Lin and J. Ni, *J. Appl. Phys.*, 2014, **116**, 044311.
5 B. Sun, Q. L. Li and P. Chen, *Micro Nano Lett.*, 2014, **9**, 468–470.
6 P. Tao, H. Guo, T. Yang and Z. Zhang, *J. Appl. Phys.*, 2014, **115**, 054305.
7 L. Ye, H. Xu, D. Zhang and S. Chen, *Mater. Res. Bull.*, 2014, **55**, 221–228.
8 M. Saab and P. Raybaud, *J. Phys. Chem. C*, 2016, **120**, 10691–10697.
9 J. Wang, F. Sun, S. Yang, Y. Li, C. Zhao, M. Xu, Y. Zhang and H. Zeng, *Appl. Phys. Lett.*, 2016, **109**, 092401.
10 H. J. Conley, B. Wang, J. I. Ziegler, R. F. Haglund Jr, S. T. Pantelides and K. I. Bolotin, *Nano Lett.*, 2013, **13**, 3626–3630.
11 H. S. Lee, S.-W. Min, Y.-G. Chang, M. K. Park, T. Nam, H. Kim, J. H. Kim, S. Ryu and S. Im, *Nano Lett.*, 2012, **12**, 3695–3700.
12 A. Newaz, D. Prasai, J. Ziegler, D. Caudel, S. Robinson, R. Haglund Jr and K. Bolotin, *Solid State Commun.*, 2013, **155**, 49–52.
13 H. Ramakrishna Matte, A. Gomathi, A. K. Manna, D. J. Late, R. Datta, S. K. Pati and C. Rao, *Angew. Chem., Int. Ed.*, 2010, **49**, 4059–4062.
14 C.-S. Park, D. Chu, Y. Shon, J. Lee and E. K. Kim, *Appl. Phys. Lett.*, 2017, **110**, 222104.
15 Y. Wang, L.-T. Tseng, P. P. Murmu, N. Bao, J. Kennedy, M. Ionesc, J. Ding, K. Suzuki, S. Li and J. Yi, *Mater. Des.*, 2017, **121**, 77–84.
16 Z. Xiang, Z. Zhang, X. Xu, Q. Zhang, Q. Wang and C. Yuan, *Phys. Chem. Chem. Phys.*, 2015, **17**, 15822–15828.
17 L. Cai, J. He, Q. Liu, T. Yao, L. Chen, W. Yan, F. Hu, Y. Jiang, Y. Zhao and T. Hu, *J. Am. Chem. Soc.*, 2015, **137**, 2622–2627.
18 Y. Wang, S. Li and J. Yi, *Sci. Rep.*, 2016, **6**, 24153.
19 N. Gao, Y. Guo, S. Zhou, Y. Bai and J. Zhao, *J. Phys. Chem. C*, 2017, **121**, 12261–12269.
20 J. Zhang, J. M. Soon, K. P. Loh, J. Yin, J. Ding, M. B. Sullivian and P. Wu, *Nano Lett.*, 2007, **7**, 2370–2376.
21 R. Shidpour and M. Manteghian, *Nanoscale*, 2010, **2**, 1429–1435.
22 X.-L. Fan, Y.-R. An and W.-J. Guo, *Nanoscale Res. Lett.*, 2016, **11**, 154.
23 S. Stoll and A. Schweiger, *J. Magn. Reson.*, 2006, **178**, 42–55.
24 H. Li, Q. Zhang, C. C. R. Yap, B. K. Tay, T. H. T. Edwin, A. Olivier and D. Baillargeat, *Adv. Funct. Mater.*, 2012, **22**, 1385–1390.
25 Z. Yang, D. Gao, J. Zhang, Q. Xu, S. Shi, K. Tao and D. Xue, *Nanoscale*, 2015, **7**, 650–658.
26 A. Panich, A. Shames, R. Rosentsveig and R. Tenne, *J. Phys.: Condens. Matter*, 2009, **21**, 395301.
27 R. Gao, W. Feng, H. Liu, B. Wang, W. Chen, G. Han, P. Zhang, H. Li, W. Li and Y. Guo, *J. Appl. Phys.*, 2003, **94**, 664–668.
28 G. Herzer, *IEEE Trans. Magn.*, 1990, **26**, 1397–1402.
29 H. Tan, W. Hu, C. Wang, C. Ma, H. Duan, W. Yan, L. Cai, P. Guo, Z. Sun and Q. Liu, *Small*, 2017, **13**. Q6
30 C.-R. Lin, Y.-M. Chu and S.-C. Wang, *Mater. Lett.*, 2006, **60**, 447–450.
31 J. Ma and K. Chen, *Sci. Rep.*, 2017, **7**, 42312.
32 M. Halder, S. Yusuf, A. Kumar, A. Nigam and L. Keller, *Phys. Rev. B: Condens. Matter Mater. Phys.*, 2011, **84**, 094435.
33 S. Roy, G. Perkins, M. Chattopadhyay, A. Nigam, K. Sokhey, P. Chaddah, A. Caplin and L. Cohen, *Phys. Rev. Lett.*, 2004, **92**, 147203.
34 A. Kumar and S. Yusuf, *Phys. Rep.*, 2015, **556**, 1–34.
35 P. Murthy, K. Priolkar, P. Bhobe, A. Das, P. Sarode and A. Nigam, *J. Magn. Magn. Mater.*, 2011, **323**, 822–828.